ACS NANO
Cite This: ACS Nano 2018, 12, 8081−8090
www.acsnano.org

ARTICLE

Giant Electron−Phonon Coupling and Deep Conduction Band Resonance in Metal Halide Double Perovskite

Julian A. Steele,[*,†] Pascal Puech,[‡] Masoumeh Keshavarz,[¶] Ruoxi Yang,[§,∥] Subhasree Banerjee,[¶,⊥] Elke Debroye,[¶] Cheol Woong Kim,[¶] Haifeng Yuan,[¶] Nam Ho Heo,[#] Johan Vanacken,[▽] Aron Walsh,[§,○] Johan Hofkens,[¶] and Maarten B. J. Roeffaers[†]

[†]Centre for Surface Chemistry and Catalysis, KU Leuven, Celestijnenlaan 200F, Leuven 3001, Belgium
[‡]CEMES/CNRS, Université de Toulouse, 29, rue Jeanne Marvig, 31055 Toulouse, France
[¶]Department of Chemistry, KU Leuven, Celestijnenlaan 200F, Leuven 3001, Belgium
[§]Department of Materials, Imperial College London, Exhibition Road, London SW7 2AZ, United Kingdom
[∥]Department of Chemistry, University of Bath, Claverton Down, Bath BA2 7AY, United Kingdom
[⊥]School of Science, Department of Chemistry, Adamas University, Barasat-Barrackpore Road, Kolkata 700126, West Bengal, India
[#]Department of Applied Chemistry, School of Applied Chemical Engineering, College of Engineering, Kyungpook National University, Daegu 41566, Korea
[▽]INPAC-Institute for Nanoscale Physics and Chemistry, KU Leuven, Celestijnenlaan 200 D, B-3001 Leuven, Belgium
[○]Global E3 Institute and Department of Materials Science and Engineering, Yonsei University, Seoul 120-749, Korea

Supporting Information

ABSTRACT: **The room-temperature charge carrier mobility and excitation−emission properties of metal halide perovskites are governed by their electronic band structures and intrinsic lattice phonon scattering mechanisms. Establishing how charge carriers interact within this scenario will have far-reaching consequences for developing high-efficiency materials for optoelectronic applications. Herein we evaluate the charge carrier scattering properties and conduction band environment of the double perovskite $Cs_2AgBiBr_6$ *via* a combinatorial approach; single crystal X-ray diffraction, optical excitation and temperature-dependent emission spectroscopy, resonant and nonresonant Raman scattering, further supported by first-principles calculations. We identify deep conduction band energy levels and that scattering from longitudinal optical phonons—*via* the Fröhlich interaction—dominates electron scattering at room temperature, manifesting within the nominally nonresonant Raman spectrum as multiphonon processes up to the fourth order. A Fröhlich coupling constant nearing 230 meV is inferred from a temperature-dependent emission line width analysis and is found to be extremely large compared to popular lead halide perovskites (between 40 and 60 meV), highlighting the fundamentally different nature of the two "single" and "double" perovskite materials branches.**

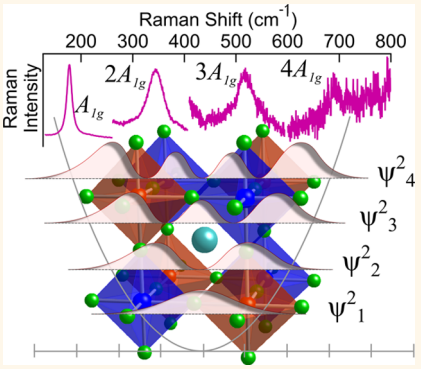

KEYWORDS: *double perovskite, $Cs_2AgBiBr_6$, Fröhlich interactions, Raman scattering, conduction band resonance*

Owing to their facile processing, low cost, and appealing optical properties, the past decade has played witness to metal halide perovskites encompassing one of the fastest growing materials ever seen within optoelectronics research.[1] In terms of their physical properties and optoelectronic performance, the lead-based perovskite systems are currently championing this pursuit; as a vivid example, single-junction solar cells based on the $FAPbI_3$ perovskite (where FA is $HC(NH_2)_2^+$) have achieved conversion efficiencies surpassing 22%[2] in just a few years, rivalling well-established Si-based technologies.[3]

Initially motivated by a desire to move away from toxic Pb-based compounds, the perovskite catalogue was recently expanded to include lead-free, so-called, "double perovskite" systems, based on an $A^I_2B^IB^{III}X_6$ architecture.[4] This new branch

Received: April 20, 2018
Accepted: August 7, 2018
Published: August 7, 2018

DOI: 10.1021/acsnano.8b02936
ACS Nano 2018, 12, 8081−8090

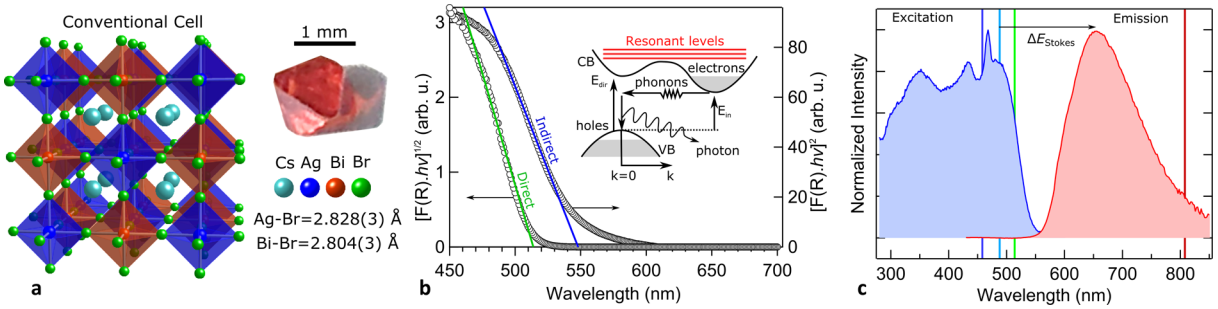

Figure 1. Structural and optical properties of single crystal $Cs_2AgBiBr_6$. (a) Optical image of a typical millimeter-sized single crystal (right) and the lattice structure of single crystal $Cs_2AgBiBr_6$ (left) derived from single crystal XRD analysis, along with the measured bond lengths for the Ag−Br and Bi−Br type bonds (numbers in parentheses here indicate the respective error values). (b) Tauc plot used to measure the indirect and direct bandgaps *via* Kubelka−Munk functions. The inset shows the optical absorption process for an indirect band structure, complete with the CB resonant levels revealed through this work. (c) Normalized excitation (λ_{em} = 650 nm) and emission (λ_{exc} = 400 nm) spectra of $Cs_2AgBiBr_6$ single crystals recorded at 300 K. For reference, the colored vertical lines drawn through the spectra here indicate the wavelengths used in the Raman scattering measurements shown in Figures 2 and 3.

offers interesting and varied physical properties, differing substantially from their Pb-based counterparts. From its conception, the highly stable[5,6] all-inorganic $Cs_2AgBiBr_6$ system quickly became a popular material for researchers.[7] With promise for its application within solar cells currently declining,[8] its immediate promise seems to reside in its strong potential for creating highly sensitive direct-conversion X-ray and γ-radiation detectors.[6]

Slavney *et al.*[9] recently reported that $Cs_2AgBiBr_6$ is an indirect bandgap material, identifying phonons with an assisting energy of $\hbar\omega$ = 0.12 eV are required to transition between the Γ and L zone boundaries defined by the valence band maximum (VBM) and conduction band minimum (CBM), respectively. Such a phonon band would possess a frequency nearing 1000 cm^{-1}, indicating that multiphonon processes are at play here, defining the strength of the optical absorption edge.[9] Moreover, recent theoretical studies[10,11] of $Cs_2AgBiBr_6$ have suggested a complex energy landscape for conduction band (CB) electrons, where orbital-induced levels from both Bi and Ag atoms might disrupt the density of states (DOS) high into the CB. How these orbitals might manifest through its carrier dynamics or optoelectronic properties is currently unknown.

The atoms in room-temperature semiconductors are not at rest, and their relative displacements from equilibrium perturb the periodic potential exerted on charge carriers, leading to carrier-phonon scattering. For double perovskite structures, compared to their single perovskite counterparts, the lattice dynamics will be inherently more complicated due to the addition of a second vibrating B-type metal halide sublattice, leading to a complex environment for which conduction electrons and carrier-phonon interactions can exist. The mechanisms of charge-carrier scattering are vitally important,[12] as they will underpin several key physical properties, like charge-carrier mobility, the size of the Stokes shift and emission line width, as well as limited thermal conductivity.[13,14] Beyond these better-known influences, it is further thought that the formation of large polarons in metal halide perovskites[15−17] which are capable of internally screening each other might in fact slow down the carrier recombination process, helping to explain the relatively prolific reporting of long carrier lifetimes across many different metal halide perovskite compounds.[1] Note that for the pertinent case of room-temperature $Cs_2AgBiBr_6$, a relatively long radiative lifetime of roughly 660 ns was reported,[9] which can be extended through photobleaching.[18] Needless to say, establishing how charge carriers interact with phonons is essential for the development of high-efficiency devices based on $Cs_2AgBiBr_6$. Thus far, intense efforts have been made for deciphering these interactions within popular lead-based perovskite systems,[2,15,19−25] and despite the importance of carrier-phonon interactions to the optoelectronic properties, clear descriptions of what scattering mechanisms are active within metal halide double perovskites are yet to appear.

We remedy this in the following article and shed light on the complex interconnectedness of the structural, vibrational, and optoelectronic properties of $Cs_2AgBiBr_6$. Using a combination of fine-structure X-ray diffraction (XRD) analysis, several optical spectroscopic techniques, and density functional theory (DFT) calculations, we outline a physical model which is characterized by giant electron−phonon coupling (so-called Fröhlich interactions) that arises *via* a highly harmonic and vibrationally dominant $(AgBr_6)^{5-}$ sublattice, as well as a collection of strongly resonant electronic states distributed above the CBM. The large Fröhlich coupling strength in $Cs_2AgBiBr_6$ is shown to be responsive to thermal annealing, reducing up to roughly 10% following treatment, and suggests that the degree of structural ordering in the double perovskite underpins the relatively strong electron−phonon interactions.

RESULTS

We begin with an overview of the important characteristic properties of phase-pure $Cs_2AgBiBr_6$.[5] In the present work, we have chosen to study single crystals of $Cs_2AgBiBr_6$ exhibiting model physical characteristics in the absence of grain boundaries. It follows that, while $Cs_2AgBiBr_6$ appears to suffer from several growth generated defects, our materials offer a preferable test bed for the evaluation of intrinsic properties.

Structural and Optical Characterization. $Cs_2AgBiBr_6$ single crystals (Figure 1a) were grown *via* the solution processing method reported previously.[9] Fine-structure single crystal XRD analysis was carried out using synchrotron X-ray radiation and is shown in Figure 1a, revealing a highly crystalline and phase-pure octahedral structure (space group $Fm\bar{3}m$), in sound agreement with literature.[9,26] Note that the complete set of structural details (Table S1) and thermal and occupancy parameters (Table S2) derived can be found in the Supporting Information. The fundamental optical absorption

DOI: 10.1021/acsnano.8b02936
ACS Nano 2018, 12, 8081−8090

edge was probed by UV−vis diffuse reflectance spectroscopy, with the analyzed spectra converted in Figure 1b *via* the Kubelka−Munk function, $F(R)$. Assessing the degree of linearity of our data scaled using both indirect-Tauc ($[F(R)\cdot h\nu]^{1/2}$ *vs* nm) and direct-Tauc ($[F(R)\cdot h\nu]^2$ *vs* nm) plots, we determine the respective bandgap transitions to be 550 nm (2.25 eV) and 514 nm (2.41 eV). The value of the indirect bandgap is comparable to other reports which range from 677 nm (1.83 eV) to 566 nm (2.19 eV).[5,8,26−28] Isolating the origin(s) of the relatively large spread in E_g values observed here is difficult, although the answer likely resides in the different methods employed to probe the band structure, which exhibits an extremely large Stokes shift (see Figure 1c) and the variances in synthesis conditions. Recent work by Yang *et al.*[29] has suggested that the ordering parameter in the double perovskite can lead from a larger indirect bandgap (fully ordered) to a smaller pseudodirect one (fully random ordering). Thus, combined with the narrow growth window of $Cs_2AgBiBr_6$,[30] a wider bandgap is concomitant with a more ordered system with less Ag-on-Bi (Ag_{Bi}) or Bi-on-Ag (Bi_{Ag}) antisites.[6]

Next, we study the properties of photogenerated states in $Cs_2AgBiBr_6$ by assessing its steady-state excitation and photoluminescence (PL) properties, which is shown in Figure 1c. The PL spectrum of $Cs_2AgBiBr_6$ here exhibits a wide and smooth emission centered near 650 nm, while the excitation spectrum is characterized by a very broad response, suggesting multiple photoexcited states that are widely distributed in energy. Moreover, the excitation line shape—with the inclusion of sharp peak-like features—further suggests some of these states to be discrete-like, existing above the absorption edge and well into the CB. On the origin of the above bandgap energy levels in $Cs_2AgBiBr_6$, several recent reports[10,11] provide sound theoretical support for their discussion. In short, DFT calculations accounting for the influence of spin−orbit coupling have indicated that the CBM of ordered[29] $Cs_2AgBiBr_6$ is composed mainly of Bi 6p orbitals, with some additional contributions from the Ag 5s and Br 4p orbitals.[10] This electronic structure governs the energy landscape which photogenerated electrons can be excited from the ground state into the CB, where these orbitals are further split due to spin−orbit coupling.[10] Electronic transitions in the $Cs_2AgBiBr_6$ will couple to lattice vibrations, acting to broaden the emission band and enlarge the Stokes shift energy, E_{Stokes}. Together, the relatively large Stokes shift and large emission line width seen in $Cs_2AgBiBr_6$ are an indicator of strong anharmonicity.

Evaluation of Lattice Dynamics. To study the nature of phonon vibrations in $Cs_2AgBiBr_6$, its lattice dynamics were calculated using DFT *via* the PBEsol exchange−correlation functional and a harmonic approximation[31] (anharmonicity not considered), with the determined zone center phonon DOS for $Cs_2AgBiBr_6$ presented in Figure 2a. Jahn−Teller distortions constitute a good portion of the vibrational states seen here, which is common for a highly mobile perovskite structure. Unsurprisingly, given the relatively heavy elements involved, the first-order phonons contain only relatively low-energy vibrations, all residing far below 200 cm^{-1} (note that the DFT calculation determined properties at 0 K, so frequencies measured at room temperature will be inherently larger).

For the vibrational symmetry analysis of the $Cs_2AgBiBr_6$ crystal structure (O_h symmetry), parallels can be drawn to other analogous elpasolite perovskites; see inset of Figure 2b. A

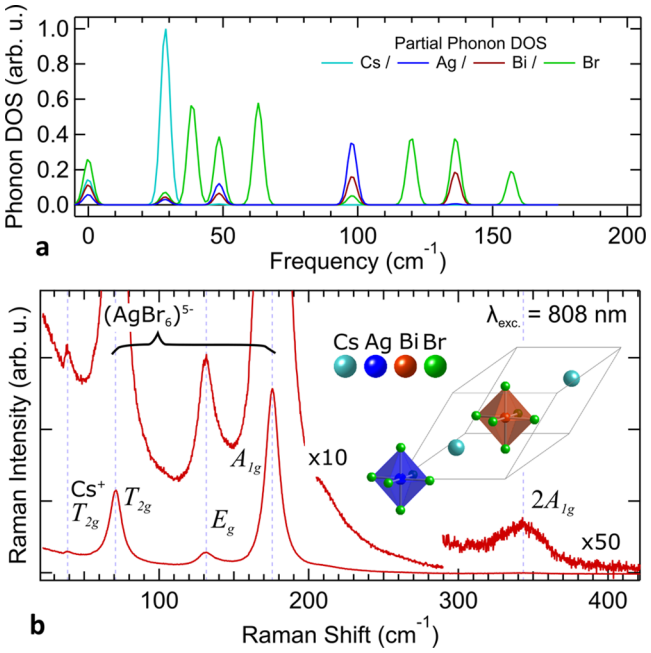

Figure 2. Lattice dynamics of $Cs_2AgBiBr_6$. (a) DFT calculation of the partial phonon DOS at the zone center (Γ) for $Cs_2AgBiBr_6$ at 0 K, using a smearing factor of 2 cm^{-1}. (b) Nonresonant Raman spectrum recorded using 808 nm excitation, with the inset showing a representation of the primitive cell, whereby the two octahedral sublattices (O_h symmetry) and Cs^+ ions (T_d symmetry) are separated.

complete factor group analysis is developed on the basis of the Bravais cell, which is used to predict the vibrational symmetries of $Cs_2AgBiBr_6$ (see Table S3). Analyzing the XRD data in Figure 1a to assess the relative internal forces of the two competing $(AgBr_6)^{5-}$ and $(BiBr_6)^{3-}$ octahedral bonds, we find that the relative strength of the Ag−Br and Bi−Br bond types strongly differ. This is concluded from a comparison to the measured bond lengths (Figure 1a) of Ag−Br (2.828 Å) and Bi−Br (2.804 Å) and their calculated ionic radii: For the 6-coordinated B−Br types (B = Bi or Ag), we have Bi−Br = 2.99 Å and Ag−Br = 3.11 Å. The ionic radius of Ag is larger than that of Bi, though the recorded bond lengths for the two bond types are very comparable. Bonding distortions will arise in the double perovskite because of the large mismatch of the two sublattices, through strain relaxation, whereby the system must compensate by modifying bonding lengths. In the present case, the strain appears to be mostly compensated at the Ag−Br type bond, evidenced by its relatively larger compression.

In this way, the bonding strength of the Ag−Br type bonds is found to be much stronger than that of the Bi−Br ones, permitting it to be considered a discrete-like entity. Under these circumstances, the $(AgBr_6)^{5-}$ lattice vibrations dominate and the $(BiBr_6)^{3-}$ Raman modes will turn silent. It follows that four active first-order modes are anticipated in the nonresonant Raman scattering spectrum. These vibrational modes consist of a single low-energy vibration which is a translational mode due to the "caged" Cs^+ ions, and three higher energy modes corresponding to a single breathing and two stretching vibrations arising from the $(AgBr_6)^{5-}$ sublattice.

The room-temperature nonresonant Raman spectrum measured using 808 nm laser light is presented in Figure 2b, with the relative wavelengths used for all Raman excitations within this paper indicated in Figure 1c. Here we see a total of

DOI: 10.1021/acsnano.8b02936
ACS Nano 2018, 12, 8081−8090

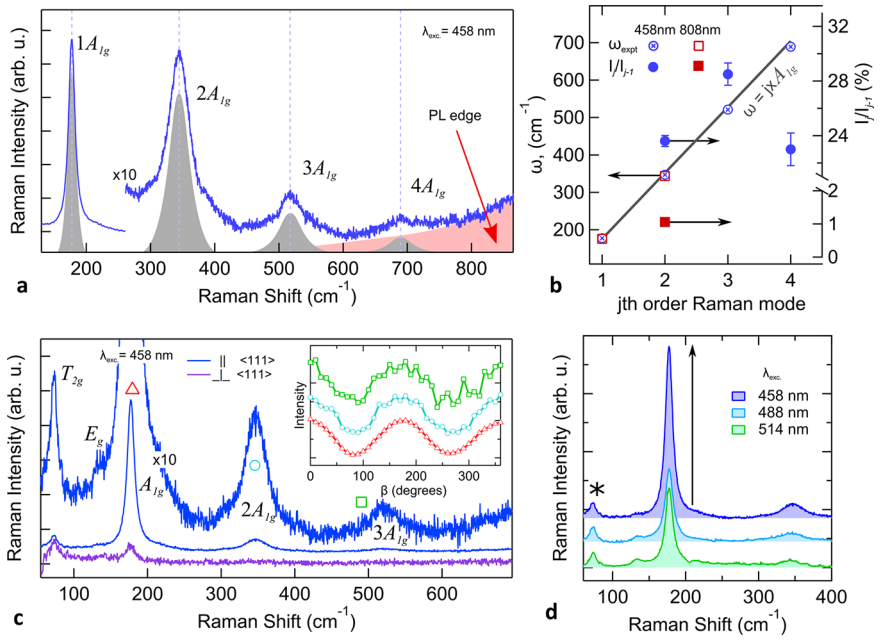

Figure 3. Quasi-resonant and polarized Raman scattering studies of $Cs_2AgBiBr_6$. (a) Unpolarized Raman spectrum recorded using 458 nm excitation, highlighting observations of up to the fourth A_{1g} harmonic, before Raman signals are lost to the high-energy shoulder of the PL emission. (b) Frequency and relative intensity of harmonic Raman modes. (c) Comparison of polarized Raman backscattering spectra recorded using 458 nm excitation and polarizing optics parallel and perpendicular to the ⟨111⟩ crystal direction, with the inset showing the full analyzed rotation made with the polarization of the incident light fixed along ⟨111⟩. The traces in the inset have been offset and normalized for clarity. (d) Comparison of pseudoresonant Raman scattering effect (normalized to the mode at 75 cm^{-1}, indicted by "*") made with three different excitation energies across the absorption edge (see positions of excitation relative to excitation spectrum in Figure 1c).

four bands below 200 cm^{-1}, as expected from our group factor and fine-structure analysis, with their intensity and frequency in complete agreement with that measured from other elpasolite systems.[32−34] According to our assignment, the narrow low-frequency band at 40 cm^{-1} is ascribed to the T_{2g} mode of the Cs^+ ions, while the three other more intense bands at 75, 135, and 175 cm^{-1} belong respectively to the T_{2g} (breathing), E_g, and A_{1g} (both stretching) modes of the $(AgBr_6)^{5-}$ octahedron, given that the following general relation[34] is satisfied: $\nu^2_{A_{1g}} \approx \nu^2_{E_g} + \frac{3}{2}\nu^2_{T_{2g}}$.

The $Cs_2AgBiBr_6$ double perovskite system remains to exhibit phase purity issues, mainly due to its narrow growth window and a tendency to form a Bi-rich yellow-colored side phase.[5] During the optimization stage of producing our high phase purity $Cs_2AgBiBr_6$ single crystals, the yellow phase was on occasion inadvertently synthesized, and we provide its characterization using energy-dispersive X-ray spectroscopy (Figure S1; showing the material to be Bi-rich) and Raman spectroscopy (Figure S2; identifying its unique Raman modes) in the Supporting Information. With sound alignment between their vibrational energies, comparison of the Raman spectrum recorded from our Bi-rich yellow phase material with that reported for $Cs_3Bi_2Br_9$[35] indicates that this is its composition. Where XRD unavoidably requires bulk characterization and might potentially miss the presence of microscopic trace amounts of the second yellow phase, we emphasize that the vibrational signatures of the yellow phase can provide a relatively straightforward and reliable probe for evaluating localized deviations in phase purity within single crystals. To demonstrate how this might work, we provide, in Figure S3 of the Supporting Information, a micro-Raman surface map of a $Cs_2AgBiBr_6$ single crystal suffering phase purity problems. As interpreted by the Raman analysis, the measurement confirms the presence of localized areas of the yellow phase peppered throughout the $Cs_2AgBiBr_6$ single crystal.

Phonon Coupling and the Stokes Shift. In polar semiconductors, an important scattering mechanism is the Fröhlich interaction, which represents the coupling of longitudinal optical (LO) phonons to lattice vibrations *via* Coulomb interactions. Here we identify the LO phonon to have A_{1g} symmetry and an energy of $\hbar\omega_{LO}$ = 175 cm^{-1}, whereby the Fröhlich interaction should dominate at room temperature,[22] given that the LO phonon occupation number is high; $k_BT \gg \hbar\omega_{LO}$. The interactions between optical centers and LO modes may be characterized by the Huang−Rhys factor, S, which represents (i) the average number of vibrations emitted after an optical transition between excited and ground states and (ii) an indicator of the coupling strength. The Huang−Rhys parameter follows the standard form of a configuration coordinate diagram and is approximately[36] related to the Stokes shift energy *via* $\Delta E_{Stokes} = 2S\hbar\omega_{LO}$. Using the measured energy shift seen between the emission and excitation bands of $Cs_2AgBiBr_6$ in Figure 1c (*i.e.*, $\Delta E_{Stokes} \sim 0.7$ eV), we arrive at the relatively large Huang−Rhys value of S = 15.4, confirming the presence of strong Fröhlich interactions.

Higher Order Raman Active Harmonics. Interestingly, in the nonresonant 808 nm excited Raman spectrum shown in Figure 2b, an additional weak band is clearly resolved at higher energies on the ×50 rescaled trace. With no high-energy modes expected from the first-order phonon DOS calculated in Figure 2a, such a band likely arises from higher order phonon combinations. Assessing its observed vibrational energy to be 346 cm^{-1}, we find it to reside just short of double the A_{1g} mode

DOI: 10.1021/acsnano.8b02936
ACS Nano 2018, 12, 8081−8090

at 175 cm^{-1}, indicating it may possibly have a strong $2A_{1g}$ component. We note that nonresonant overtones are not unexpected in polar crystals which exhibit relatively large carrier-phonon coupling, but are actually unusual within the modern metal halide perovskites.

To examine if the 346 cm^{-1} mode comes from second-order scattering of A_{1g} phonons, we evaluate its Raman response using highly absorbing above-bandgap excitations and search for the presence of higher order bands. In Figure 3a we present the higher energy portion of the Raman spectrum recorded using a relatively low 458 nm laser power density to avoid laser damage (see Figure S4) and highlight clear observations of several other vibrations nearing 700 cm^{-1}. In Figure 3b, the measured frequencies of these bands (identified as jth order modes) are compared to that expected from consecutive A_{1g} overtones (solid straight line). The position of these bands is in reasonable agreement with the predicted A_{1g} combinations, all the way up to a remarkable *fourth-order* observation.

Next we unambiguously confirm the common A_{1g} vibrational symmetry of the high-energy modes revealed *via* the Raman selection rules and through implementing polarized measurements. Polarizing the incident light along the ⟨111⟩ direction of a $Cs_2AgBiBr_6$ single crystal, and analyzing polarized scattered light rotated around the (111) plane (forming the relative polarization angle β) constitutes the data shown in Figure 3c. First, at polarization geometries both parallel (β = 0) and perpendicular (β = 90 °C) to the ⟨111⟩ crystallographic direction, oscillators identified by combinations of A_{1g} are all active and nonactive, respectively, confirming their shared symmetry. The full rotation analysis of this measurement is also contained in the inset of Figure 3c, where the normalized and offset intensities of the three modes are shown to coincide throughout the full rotation, further verifying their shared origins.

The measured frequencies of the A_{1g} harmonics in Figure 3b do deviate slightly, being in the vicinity of 2−3% less than their respective first-order A_{1g} multiples, suggesting vibrational contributions to centrally come from the Γ point.[37] As well, the relatively large broadening of the higher order peaks (a full width half-maximum of roughly 10 cm^{-1} at j = 1, to roughly 40 cm^{-1} at j = 2−4) and its relative deviation toward lower frequencies both suggest additional contributions of A_{1g} phonons from other points of the Brillouin zone;[14] the participation of ordinarily forbidden $k \neq 0$ phonons in these multiphonon processes might explain their relatively large widths.

On the scaling used to present the Raman data in Figure 3a,c, it is clear that the relative oscillator strength of the consecutive overtones are large and substantially larger than that measured using 808 nm excitation (see Figure 2b). The selective nominally nonresonant enhancement of optical overtones will require the presence of relatively strong electron−phonon Fröhlich interactions[38] within $Cs_2AgBiBr_6$. A quantification of the relative oscillator strength is further contained in Figure 3b, where the intensity of the jth mode (I_j) is compared relative to jth − 1 (I_{j-1}), and is roughly 1% when using 808 nm light, however jumps closer to 30% when using above bandgap 458 nm excitation, up to the recorded fourth-order mode. We point out this trend explicitly overshoots theoretical considerations for such Raman multiphonon behavior[39] and is in fact a central parameter leading to the spectroscopic quantification of an extremely large carrier-phonon coupling strength,[20,38] that is, the intensity of the second-order mode relative to the first will be proportional to the Huang−Rhys parameter, S. Note that the semiconductor response to the excitation laser energy used significantly complicates an analysis of the carrier-phonon coupling strength here, and a detailed examination is still to come. As such, a spectral analysis breaks down due to the strong emergence of third-order and fourth-order A_{1g} bands, suggesting the occurrence of resonance effects. This is in contrast to the position of the excitation energy relative to the CBM in Figure 1b; the excitation should be well above the CBM and away from resonance. Presumably, the third- and fourth-order overtones arise in the current case from resonant conditions being partially satisfied, in the presence of deep CB energy levels.

In Figure 3d, the influence of varying the Raman excitation energy is examined. While typical resonant Raman scattering experiments aim to match the excitation energy with fundamental interband transitions of the semiconductor, here we aim to probe resonant levels deep within the CB of $Cs_2AgBiBr_6$. For the change in excitation conditions, we point out that negligible spectral changes are seen for different populations of photoinjected charge carriers, and all measurements were performed using a low laser power density (∼0.1 kW/cm^2). Compared to the excitation spectrum recorded in Figure 1c, the relative positions of the exciting 458, 488, and 514 nm photons are indicated for reference by the vertical lines in the same plot. Unpolarized Raman data are recorded at these wavelengths and are compared in Figure 3d *via* a normalization to their respective T_{2g} symmetry vibrations near 75 cm^{-1}. For these data, a correction has been applied to the spectral background for those recorded using 488 and 514 nm light, given their relative proximity to the high-energy shoulder of the PL emission which defines the background (see Figure S5). In doing so, we see a substantial rise in the relative scattering cross-section of the A_{1g} and $2A_{1g}$ modes, relative to the T_{2g} band, when employing different photon energies traversing the absorption edge (see Figure 1c). The relative weightings of both the A_{1g} and $2A_{1g}$ roughly triple here when moving from 488 to 458 nm. Further, through an analysis of the relative weights of the second- and first-order bands, we find there is also a sharp spike in the relative overtone intensity when moving from 514 nm (0.11) to 488 or 458 nm (both being ∼0.25). In fact, from the charge density isosurface calculations reported by Savory *et al.*,[8] the electron density in the CB is mainly localized near the metal atoms of the crystal lattice, providing efficient electron−phonon coupling to orbit-induced levels. Being directly proportional to the Huang−Rhys coupling strength, S, the spectral variations seen here reflect a shift in the resonance conductions and verifies the notion of photogenerated electrons being promoted into localized states well above the CBM.

Temperature Dependence of PL Emission Line Width. To quantify the relative activity of different charge-carrier scattering mechanisms in $Cs_2AgBiBr_6$, we investigate the temperature dependence of the emission line width, which constitutes the data presented in Figure 4. To provide details useful for its analysis, a comparison of the Raman spectrum of $Cs_2AgBiBr_6$ recorded at 80 and 300 K (808 nm excitation) is presented in Figure S6. Within this comparison, very little spectral differences are seen, indicating the cubic structure and relative bonding strength at lower temperatures is persevered and extends a practical application of our analysis up to room temperature. Further, we exact the energy of the low-

DOI: 10.1021/acsnano.8b02936
ACS Nano 2018, 12, 8081−8090

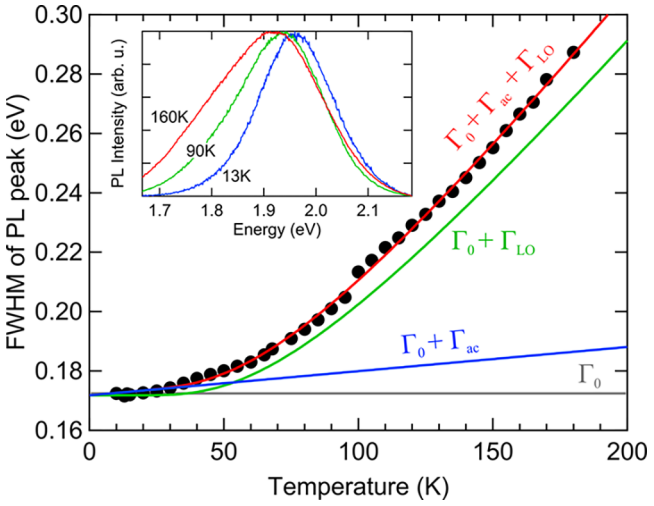

Figure 4. Temperature dependence of $Cs_2AgBiBr_6$ emission line width. The fwhm of single crystal $Cs_2AgBiBr_6$ steady-state PL spectra as a function of temperature, with an example of measured raw data spectra provided in the inset for several different temperatures. The red line is a fit made with eq 1 using the parameters Γ_0 = 171.8 meV and $\hbar\omega_0$ = 22 meV, while the measured contributions to the line width broadening induced by acoustic and LO phonon (Fröhlich interactions) coupling are parsed *via* the blue and green traces, respectively.

temperature optical phonon involved, that is, $\hbar\omega_{LO}$ is measured to be 22 meV.

Heading to lower temperatures in Figure 4, the PL emission narrows significantly from fwhm = 285 meV at 180 K down to 173 meV at 10 K, as highlighted by the PL spectra contained in its inset. Such a monotonic dependence on temperature is relatively well understood for semiconducting materials[22,40] and is compactly described by the eq 1 below, where we have chosen to adopt the nomenclature used by Wright *et al.*[22] Within the broadening model implemented in our work, where we ignore the negligible trend of scattering from ionized impurities,[22,41] which is not expressed in our data, two central temperature-dependent parameters act functionally different to widen the emission line width above absolute zero, being described by

$$\Gamma(T) = \Gamma_0 + \Gamma_{ac} + \Gamma_{LO} = \Gamma_0 + \gamma_{ac}T + \gamma_{LO}n(T) \quad (1)$$

where Γ_0 is a constant and represents the temperature-independent inhomogeneous broadening parameter originating due to scattering from disorder and/or crystallographic imperfections. The next two terms provide the important temperature dependence: Γ_{ac} and Γ_{LO} are the acoustic and optical phonon (Fröhlich) interactions with carrier-phonon coupling constants γ_{ac} and γ_{LO}, respectively. Given the LO phonon energy in $Cs_2AgBiBr_6$ is 22 meV, its population below 100 K will be small, being governed by the Bose–Einstein distribution $n(T) = 1/(\exp(\hbar\omega_0/k_BT) - 1)$. Thus, one can expect that the emission broadening in this temperature regime will contain significant contributions from the scattering of acoustic phonons.[42] In parsing the two contributions to broadening, we find the best fits to our data are made accounting for the γ_{ac} at the low-temperature regime. Extrapolating the data in Figure 4 to 0 K, we estimate a relatively large[22] natural line width of Γ_0 = 171.8 ± 0.5 meV, suggesting a substantial intrinsic defect population.

Inputting these parameters into eq 1 one arrives at the following electron coupling constants: γ_{ac} = 81 ± 16 μeV and γ_{LO} = 226 ± 14 meV. This directly confirms a relatively large electron–phonon Fröhlich interaction within $Cs_2AgBiBr_6$, being several times larger than that reported for several popular organic lead halide perovskites;[22] namely, the four variants of $(FA,MA)Pb(I,Br)_3$, having γ_{LO} values in the order of 40–60 meV. From our data, it can be concluded that Fröhlich coupling to LO phonons is the major cause of line width broadening in $Cs_2AgBiBr_6$ at room temperature, with scattering from acoustic phonons and impurities being far less important. This result is in complete agreement with a classic band structure picture for a polar inorganic semiconductor and in alignment with other hybrid Pb-based perovskites.[22]

Fröhlich Interaction Strength from First-Principles. For comparison, we assess the carrier-LO-phonon coupling strength in $Cs_2AgBiBr_6$ from first principles; in polar semiconductors the full electron–phonon coupling problem can be approximated by the interaction of carriers with a long-wavelength longitudinal optical phonon as described by the unitless Fröhlich parameter, α. This parameter is one component of the coupling strength and has been used as a comparative indicator for the Fröhlich interaction strength.[25,43] Here we adopt the approach detailed by Frost[43] for calculating the Fröhlich coupling strength of both electrons and holes:

$$\alpha = \frac{1}{4\pi\epsilon_0}\frac{1}{2}\left(\frac{1}{\epsilon_\infty} - \frac{1}{\epsilon_S}\right)\frac{e^2}{\hbar\Omega}\left(\frac{2m_b\Omega}{\hbar}\right)^{1/2} \quad (2)$$

where ϵ_∞ is the optical dielectric constant, ϵ_S is the static dielectric constant, m_b is the carrier effective mass (in units of free electron mass, m_0) and, respectively, is taken[44] for electrons and holes as 0.29 and 0.47, and Ω is the characteristic phonon angular frequency. Parameters ϵ_∞ and ϵ_S have been calculated using density functional perturbation theory (10 × 10 × 10 k-point and 800 eV plane-wave cutoff) and determined to be 5.42 and 16.73, respectively. For the effective phonon frequency, we have the Hellwarth scheme to sum over the infrared activity of all phonon branches[25,45] and use the value 3.703 THz. Note that the phonon frequencies are calculated in harmonic approximation and exclude finite-temperature effects. At elevated temperatures, the effective phonon frequency can shift due to anharmonicity and the population of higher energy modes. Through eq 2 we estimate the Fröhlich parameters for electrons and holes in $Cs_2AgBiBr_6$ to be 2.54 and 2.00, respectively. Relative to many other perovskite semiconductors, this calculation places the carrier-phonon coupling strength of $Cs_2AgBiBr_6$ well within the "intermediate" range[25] (see Frost[43] for a useful comparison of this parameter across many different material systems), and certainly not into a regime which can be identified as "strong".

The first-principles calculation of the carrier-phonon coupling strength is of course in direct conflict to the collective evidence outlined above, where a notably strong Fröhlich coupling strength in $Cs_2AgBiBr_6$ is revealed experimentally. In reconciling this large difference, we find precedence for similar disagreements between experiments[22] and theoretical calculations[43] within the literature. While parameters α and γ_{LO} cannot be compared directly, one might compare their relative magnitudes across different materials. For example, the relative magnitudes of α calculated by Frost[43] for perovskite systems

DOI: 10.1021/acsnano.8b02936
ACS Nano 2018, 12, 8081–8090

$MAPbI_3$ (α = 2.39) and $MAPbBr_3$ (α = 1.69) are in the reverse order when compared to the γ_{LO} coefficients experimentally measured for the same perovskites:[22] $MAPbI_3$ (γ_{LO} = 40 meV) and $MAPbBr_3$ (γ_{LO} = 58 meV).

This highlights the delicate nature by which first-principle calculations and experimental measurements may be compared for this problem. The origin of the large mismatch in the present study likely resides in the fact that the crystal structure simulated here assumes the perfect ordering of Ag- and Bi-type sublattices (*i.e.*, perfect checkerboard-like structure). In reality, disorder will exist in the distribution[6] of the two B-site metals present in the double perovskite; charged antisites will introduce localized fluctuations in the electrostatic potential, which can act to increase carrier-lattice coupling. In such a scenario, even a relatively small population of charged B-type antisites within a double metal halide perovskite should have a considerable effect. Note that, with regards to the emission line width shown in Figure 4, disorder is suggested by our determination of a relatively large[22,41] natural width of $\Gamma_0 \sim$ 172 meV.

Within this framework, one would expect that increasing the structural order in the system will be paralleled by a reduction in the measured Fröhlich coupling constant, γ_{LO}. Pan *et al.* demonstrated[6] that both the lattice ordering and PL emission properties of $Cs_2AgBiBr_6$ are responsive to relatively mild thermal annealing treatments. Thus, to examine potential links between the Fröhlich coupling magnitude and the lattice ordering, single crystal $Cs_2AgBiBr_6$ was mounted on heating stage inside a nitrogen-filled custom housing. An optical fiber was coupled inside, permitting the changes in the PL spectra to be recorded before and after annealing the material (160 °C for 1 h) under nitrogen. The temperature-dependent line width analysis of these experiments are contained in Figure S7 and indicates that the magnitude of γ_{LO} is indeed sensitive to a thermal treatment, reducing from 226 meV before annealing to 201 meV after. Further, we find the value of Γ_0 is unchanged by the treatment, highlighting the relatively sensitive nature by which disorder disturbs the electron scattering mechanisms, rather than the energy distribution of optical centers (*i.e.*, represented by the natural line width). The over 10% drop in the measured coupling strength strongly supports the notion that lattice disorder influences Fröhlich interactions within $Cs_2AgBiBr_6$, a feature not accounted for in the DFT modeling. Moreover, these experiments prescribe a straightforward method for controlling the electron−phonon coupling strength within double perovskite $Cs_2AgBiBr_6$, *via* a relatively mild thermal annealing treatment.

DISCUSSION

Within a technological context, the implications of this work are substantial. For the specific applications of $Cs_2AgBiBr_6$ for solar cells or light-emitting devices (LEDs), strong carrier-phonon coupling typically leads to increased carrier scattering during transport and limits mobility at room temperature. The high defect tolerance exhibited by lead halide perovskites—responsible for their excellent optoelectronic properties—have been explained by the formation of large polarons within its soft, polarizable crystal lattice.[15] This unique property has led to the proposal[16,46] that such carrier properties can dynamically screen Coulombic potentials, thus minimizing charge carrier scattering with defects, with other charges, and with LO phonons. However, large polaron formation has been associated with a marked reduction in hot carrier cooling rates,[17] while recent studies have revealed $Cs_2AgBiBr_6$ to be characterized by fast hot carrier cooling.[47] This suggests that such effects may not be present in the double perovskite $Cs_2AgBiBr_6$. Conversely, experimental and theoretical reports have recently proposed different mechanisms for charge carrier binding in metal halide perovskite materials, involving the self-trapping of electrons[48] or holes[49] through the formation of *small* polarons. Considering the implications of our model based on a disorderly double perovskite crystal lattice, this cannot be overlooked in accurately describing the transport properties of carriers in $Cs_2AgBiBr_6$ and may help explain its intrinsic p-type behavior at room temperature.[6] As such, the measured carrier mobilities within $Cs_2AgBiBr_6$ are relatively low,[6] likely leading to increased loss of carriers through nonradiative recombination and lowering overall device performance, as a result of reducing both the carrier injection and transport efficiencies. Very recently, the potential for a $Cs_2AgBiBr_6$ single junction solar cell was demonstrated,[5,50,51] achieving fairly decent diffusion lengths, however only achieving conversion efficiencies between 1 to 2.5%. Moreover, the strong broadening of emission line widths due to phonon coupling will have consequences for the color purity of light emitters.

On the other hand, for applications such as sensitive high-energy photon (X-rays and γ-radiation) detection,[6] heavy-Z semiconductors with long carrier lifetimes, and relatively high resistivities are in fact extremely desirable for suppressing the dark current under exposure to extremely high external fields (100s of volts). Further, strong electron−phonon coupling was recently found to be fundamental in the production of THz radiation from perovskites following photoexcitation,[52] offering new prospects for cheap and easy-to-make solid-state THz sources.

The implications of the deep CB resonance exhibited in $Cs_2AgBiBr_6$ single crystals are yet to be addressed. The nature of the energy levels is to locally modify the DOS for conduction electrons, moving toward a more discrete-like system. A likely consequence for electrons existing at resonance is to have their effective mass increased. Parallels can be drawn here to the ternary III−V semiconductor $GaAs_{1-x}N_x$ which also experiences resonance above its CBM, introduced *via* N-derived energy levels. In this case, an increase in the effective mass of conduction electrons is observed.[53] In $Cs_2AgBiBr_6$, an increase in the effective mass could help explain the high order of Raman overtones seen in Figure 3a, in that the Fröhlich interaction will scale with the effective mass, through eq 2. Additionally, this will also impede the mobility of electrons residing at the orbital levels, however, their energies are, from a theoretical point of view,[10] relatively far from typical transport states existing near the CBM. Ultimately, the orbital-induced levels manifest as the anomalous energy-dependent spectroscopic features observed here and are typically not seen in other Pb-based perovskite semiconductors, which possess a "smoother" CB.

CONCLUSION

In summary, we have presented a fundamental study into the properties of conduction electrons in $Cs_2AgBiBr_6$. Through a combination of several different techniques, the complex interconnectedness of the structural, vibrational, and electronic properties of $Cs_2AgBiBr_6$ is elucidated. Specifically, fine-structure XRD showed that the $(AgBr_6)^{5-}$-type octahedra dominate the internal bonding forces and, as a consequence, a

DOI: 10.1021/acsnano.8b02936
ACS Nano 2018, 12, 8081−8090

full resolving of the Raman spectrum demonstrates the lattice dynamics are dominated by vibrations from the $(AgBr_6)^{5-}$ sublattice. Excitation spectroscopy revealed the presence of metal orbital-induced energy levels existing above the CBM, confirmed by quasi-resonant Raman experiments using above bandgap light and revealed strong LO mutliphonon combinations up to the fourth order. The electron−phonon scattering mechanisms in $Cs_2AgBiBr_6$ were evaluated through temperature-dependent PL line width analysis, and strong contributions are attributed to electron−phonon Fröhlich interactions, which dominate at room temperature and account for the relatively large Stokes shift, broad emission, and poor carrier transport. First-principles studies into the Fröhlich coupling interactions suggest that the coupling strength within $Cs_2AgBiBr_6$ should fall in the intermediate range, in conflict with the parameters inferred *via* experiments. Evaluating the Fröhlich strength following a thermal annealing treatment suggests that localized electrostatic fluctuations at either metal B-site (caused by structural disorder) act to enhance the carrier-lattice coupling, highlighting the fundamentally different nature of the two "single" and "double" perovskite materials branches.

METHODS

Synthesis of Single Crystal $Cs_2AgBiBr_6$. Materials were grown according to procedure reported by Slavney *et al.*[9] A mixture of 1.0 mmol of $BiBr_3$ (≥98%, Sigma-Aldrich) and 2.0 mmol of CsBr (99.9%, Sigma-Aldrich) in 10 mL of HBr (≥99.99%, 48 w%, Honeywell Fluka) in a 40 mL vial was sonicated for 5 min. After adding 1.0 mmol AgBr (≥99%, Chem-Lab), the suspension was sonicated a further 5 min and then heated to 120 °C to dissolve the salts to a level of supersaturation. The mixture was kept at 120 °C for 3 h and then cooled by 2 °C/h to 100 °C, followed by slower cooling at a rate of 1 °C/h to 50 °C. At that time, mm-sized single crystals could be observed and collected from the mixture by filtration. The crystals were washed with isopropanol and then dried in a vacuum oven at 50 °C. Concentrated 2-propanol (HPLC, Sigma-Aldrich), dimethyl sulfoxide (DMSO) (anhydrous, ≥ 99.9%, Sigma-Aldrich), and methanol (MeOH) (anhydrous, 99.8%, Sigma-Aldrich) were used without any dilution. The solvents were either of technical grade or higher quality. Synthesis was performed under normal atmospheric condition.

Single Crystal X-ray Diffraction. Diffraction intensities for the single crystal were measured with synchrotron X-radiation *via* a silicon (111) double crystal monochromator with 0.6300 Å wavelength. The BL2D-SMDC program was used for data collection by the omega scan method. Highly redundant data sets were harvested by collecting 72 sets of frames with a 5° scan and an exposure time of 1 s per frame. The HKL3000 program, including the automated indexing program DENZO, was used to prepare the basic data files. These were corrected for Lorentz and polarization effects; negligible corrections for crystal decay were also applied. For structure determination, full-matrix least-squares refinements (SHELXL2016) using the space group $Fm\bar{3}m$ were done using all unique reflections measured. Atomic scattering factors for neutral atoms and the atomic parameters of the previous literature were used initially.[9] Anisotropic thermal parameters for all atoms and fixed weights were applied.

UV−vis Diffuse Reflectance Spectroscopy. Diffuse reflectance spectra (DRS) were recorded in the wavelength range between 200 and 800 nm with a PerkinElmer Lambda 950 UV−vis spectrophotometer. As reference, $BaSO_4$ powder was used. Crystals were crushed to a very fine powder and placed in a quartz cuvette with 1 mm path length, sealed with a Teflon stopper. Cuvettes were mounted in an integrating sphere equipped with a spectrophotometer to align the incidental light beam perpendicular to the sample. The diffused reflectance (R) was converted to $F(R)$ using the Kubelka−Munk function: $F(R) = (1 - R)^2/2R$.

Emission and Excitation Spectroscopy. Emission and excitation spectra were recorded in front-face mode with an Edinburgh Instruments FLS 920 fluorescence spectrophotometer. Single crystals were squeezed between two quartz plates (Suprasil), or the powdered sample was mounted in a quartz cuvette with 1 mm path length (similar to the DRS measurements). Measurements were performed in front face reflection mode, with a 400 nm long pass glass filter used for any signal above 410 nm to avoid second-order excitation interference. The acquired signal was corrected for using the transmittance of this filter.

Low-Temperature PL Spectroscopy. We mounted the sample on an insert in a He flow cryostat in which the temperature can be varied from 4.2 to 300 K. The sample was excited by a solid-state laser Thorlabs M365LP1 with driver DC2200 operating at 365 nm *via* a 550 μm core optical fiber. The PL spectra were collected in an increment of 5 K by 11 200 μm core optical fibers surrounding the excitation fiber and coupled to a LOT-QD Shamrock F/4 spectrometer with an electron multiplying charge-coupled detector (EMCCD) iXon DV887.

Raman Scattering Experiments. The infrared Raman measurements (808 nm) were carried out using a XY-Dilor spectrometer associated with a Ti-Sapphire (Ti:Al2O3) tunable laser which was pumped by an argon laser. The premonochromator was slightly shifted in order to approach the Rayleigh line by 20 cm^{-1}. At this wavelength, the sample is transparent and no heating effect has been observed. We used a long working distance ×40 objective with a numerical aperture of 0.4 and selected a laser power of 3 mW. A PI microcryostat able to monitor the sample temperature was set to 80 K. One face of the sample was deposited on a thermal conductive glass. Several spectral windows (typically 3) are required and have been merged giving the reported Raman spectra. Raman spectroscopy using visible wavelengths 458, 488, and 514 nm was performed on a homemade system, employing a tubale argon ion laser which is coupled into an inverted Olympus IX71 microscope. Backscattered light is passed through a TriVista triple spectrometer setup (Princeton Instruments) which used to disperse optical signals that are detected using a liquid nitrogen-cooled CCD camera. Polarization measurements were performed *via* a Fresnel rhomb and linear polarizing combination before optical backscattering, and a liner polarizer implemented prior to dispersion. Given the high optical absorbance at these wavelengths, relatively low laser powers were employed to avoid laser damage (typically <100 W/cm^2).

Computational Methods. First-principles lattice dynamics calculations were performed to calculate the vibrational spectrum of the ordered double perovskite $Cs_2AgBiBr_6$. The harmonic force constants were calculated within DFT using the PBEsol functional as implemented in the plane-wave code VASP.[54,55] The zone-center phonons and dielectric constants were obtained using density functional perturbation theory with 10 × 10 × 10 k-point mesh and 800 eV cutoff energy for the primitive unit cell. The phonon properties were processed using Phonopy.[56]

ASSOCIATED CONTENT

Supporting Information

The Supporting Information is available free of charge on the ACS Publications website at DOI: 10.1021/acsnano.8b02936.

Crystallographic information derived from single crystal XRD, group factor analysis and $Cs_2AgBiBr_6$ vibrational assignment, EDX and Raman spectroscopic mapping of the so-called yellow phase, power dependence of laser-induced $Cs_2AgBiBr_6$ surface modifications, low-temperature Raman spectrum, and a comparison of the temperature dependence of $Cs_2AgBiBr_6$ emission line width before and after thermal annealing (PDF)

DOI: 10.1021/acsnano.8b02936
ACS Nano 2018, 12, 8081−8090

AUTHOR INFORMATION

Corresponding Author

*E-mail: julian.steele@kuleuven.be.

ORCID

Julian A. Steele: 0000-0001-7982-4413
Masoumeh Keshavarz: 0000-0003-3685-6778
Cheol Woong Kim: 0000-0002-7053-9744
Haifeng Yuan: 0000-0001-6652-3670
Nam Ho Heo: 0000-0003-4689-0080
Aron Walsh: 0000-0001-5460-7033
Johan Hofkens: 0000-0002-9101-0567

Author Contributions

J.A.S. conceived and directed this study. E.D., H.Y., and S.B. grew samples and completed the excitation and emission spectroscopy. C.W.K. and N.H.H. performed the single crystal X-ray diffraction measurements, J.A.S and P.P. conducted the Raman experiments, M.K. and J.V. completed the low-temperature PL studies, and R.X.Y and A.W. performed the first-principles calculations. J.A.S., M.K., H,Y., J.H., and M.B.J.R. provided data analysis and interpretation. J.A.S. wrote the manuscript. All authors contributed to the discussion and revising of the manuscript.

Notes

The authors declare no competing financial interest.

ACKNOWLEDGMENTS

The authors acknowledge financial support from the Research Foundation-Flanders (FWO, grant nos. G.0962.13, G.0B39.15, G.0197.11, and ZW15_09 GOH6316, postdoctoral fellowships to J.A.S., H.Y., and E.D.), KU Leuven Research Fund (C14/15/053), the Flemish government through long term structural funding Methusalem (CASAS2, Meth/15/04), the Hercules foundation (HER/11/14), and the Belgian Federal Science Policy Office (IAP-VII/05). The research leading to these results has received funding from the European Research Council under the European Union's Seventh Framework Programme (FP/2007-2013)/ERC grant agreement (grant no. 307523), ERC-Stg LIGHT to M.B.J.R. C.W.K and N.H.H. acknowledge the Pohang Light Source, Korea, for the use of their diffractometers and computing facilities.

REFERENCES

(1) Chen, Q.; De Marco, N.; Yang, Y.; Song, T. B.; Chen, C. C.; Zhao, H.; Hong, Z.; Zhou, H.; Yang, Y. Under the Spotlight: The Organic-Inorganic Hybrid Halide Perovskite for Optoelectronic Applications. *Nano Today* **2015**, *10*, 355−396.

(2) Yang, W. S.; Park, B. W.; Jung, E. H.; Jeon, N. J.; Kim, Y. C.; Lee, D. U.; Shin, S. S.; Seo, J.; Kim, E. K.; Noh, J. H.; Seok, S. I. Iodide Management in Formamidinium-Lead-Halide-Based Perovskite Layers for Efficient Solar Cells. *Science* **2017**, *356*, 1376−1379.

(3) Green, M. A.; Hishikawa, Y.; Dunlop, E. D.; Levi, D. H.; Hohl-Ebinger, J.; Ho-Baillie, A. W. Solar Cell Efficiency Tables (Version 51). *Prog. Photovoltaics* **2018**, *26*, 3−12.

(4) Volonakis, G.; Filip, M. R.; Haghighirad, A. A.; Sakai, N.; Wenger, B.; Snaith, H. J.; Giustino, F. Lead-Free Halide Double Perovskites *via* Heterovalent Substitution of Noble Metals. *J. Phys. Chem. Lett.* **2016**, *7*, 1254−1259.

(5) Greul, E.; Petrus, M.; Binek, A.; Docampo, P.; Bein, T. Highly Stable, Phase Pure $Cs_2AgBiBr_6$ Double Perovskite Thin Films for Optoelectronic Applications. *J. Mater. Chem. A* **2017**, *5*, 19972−19981.

(6) Pan, W.; Wu, H.; Luo, J.; Deng, Z.; Ge, C.; Chen, C.; Jiang, X.; Yin, W.-J.; Niu, G.; Zhu, L.; Yin, L.; Zhou, Y.; Xie, Q.; Ke, X.; Sui, M.; Tang, J. $Cs_2AgBiBr_6$ Single-Crystal X-ray Detectors with a Low detection Limit. *Nat. Photonics* **2017**, *11*, 726−732.

(7) Hu, H.; Dong, B.; Zhang, W. Low-Toxic Metal Halide Perovskites: Opportunities and Future Challenges. *J. Mater. Chem. A* **2017**, *5*, 11436−11449.

(8) Savory, C. N.; Walsh, A.; Scanlon, D. O. Can Pb-Free Halide Double Perovskites Support High-Efficiency Solar Cells? *ACS Energy Lett.* **2016**, *1*, 949−955.

(9) Slavney, A. H.; Hu, T.; Lindenberg, A. M.; Karunadasa, H. I. A Bismuth-Halide Double Perovskite with Long Carrier Recombination Lifetime for Photovoltaic Applications. *J. Am. Chem. Soc.* **2016**, *138*, 2138−2141.

(10) Xiao, Z.; Meng, W.; Wang, J.; Yan, Y. Thermodynamic Stability and Defect Chemistry of Bismuth-Based Lead-Free Double Perovskites. *ChemSusChem* **2016**, *9*, 2628−2633.

(11) Du, K. Z.; Meng, W.; Wang, X.; Yan, Y.; Mitzi, D. B. Bandgap Engineering of Lead-Free Double Perovskite $Cs_2AgBiBr_6$through Trivalent Metal Alloying. *Angew. Chem., Int. Ed.* **2017**, *56*, 8158−8162.

(12) Herz, L. M. Charge-Carrier Mobilities in Metal Halide Perovskites: Fundamental Mechanisms and Limits. *ACS Energy Lett.* **2017**, *2*, 1539−1548.

(13) Petritz, R. L.; Scanlon, W. W. Mobility of Electrons and Holes in the Polar Crystal, PbS. *Phys. Rev.* **1955**, *97*, 1620−1626.

(14) Haque, E.; Hossain, M. A. Origin of Ultra-Low Lattice Thermal Conductivity in Cs_2BiAgX_6 (X = Cl, Br) and its Impact on Thermoelectric Performance. *J. Alloys Compd.* **2018**, *748*, 63−72.

(15) Miyata, K.; Meggiolaro, D.; Trinh, M. T.; Joshi, P. P.; Mosconi, E.; Jones, S. C.; De Angelis, F.; Zhu, X. Y. Large Polarons in Lead Halide Perovskites. *Sci. Adv.* **2017**, *3*, e1701217.

(16) Zhu, X. Y.; Podzorov, V. Charge Carriers in Hybrid Organic-Inorganic Lead Halide Perovskites Might Be Protected as Large Polarons. *J. Phys. Chem. Lett.* **2015**, *6*, 4758−4761.

(17) Miyata, K.; Atallah, T. L.; Zhu, X. Y. Lead Halide Perovskites: Crystal-Liquid Duality, Phonon Glass Electron Crystals, and Large Polaron Formation. *Sci. Adv.* **2017**, *3*, e1701469.

(18) Hoye, R.; Eyre, L.; Wei, F.; Brivio, F.; Sadhanala, A.; Sun, S.; Li, W.; Zhang, K.; Macmanus-Driscoll, J.; Bristowe, P.; Friend, R.; Cheetham, A.; Deschler, F. Fundamental Carrier Lifetime Exceeding 1μs in $Cs_2AgBiBr_6$ Double Perovskite. *Adv. Mater. Interfaces* **2018**, 1800464.

(19) Gong, X.; Voznyy, O.; Jain, A.; Liu, W.; Sabatini, R.; Piontkowski, Z.; Walters, G.; Bappi, G.; Nokhrin, S.; Bushuyev, O.; Yuan, M.; Comin, R.; McCamant, D.; Kelley, S. O.; Sargent, E. H. Electron-Phonon Interaction in Efficient Perovskite Blue Emitters. *Nat. Mater.* **2018**, *17*, 550−556.

(20) Iaru, C. M.; Geuchies, J. J.; Koenraad, P. M.; Vanmaekelbergh, D.; Silov, A. Y. Strong Carrier-Phonon Coupling in Lead Halide Perovskite Nanocrystals. *ACS Nano* **2017**, *11*, 11024−11030.

(21) Fu, J.; Xu, Q.; Han, G.; Wu, B.; Huan, C. H. A.; Leek, M. L.; Sum, T. C. Hot Carrier Cooling Mechanisms in Halide Perovskites. *Nat. Commun.* **2017**, *8*, 1300.

(22) Wright, A. D.; Verdi, C.; Milot, R. L.; Eperon, G. E.; Pérez-Osorio, M. A.; Snaith, H. J.; Giustino, F.; Johnston, M. B.; Herz, L. M. Electron-Phonon Coupling in Hybrid Lead Lalide Perovskites. *Nat. Commun.* **2016**, *7*, 11755.

(23) Sendner, M.; Nayak, P. K.; Egger, D. A.; Beck, S.; Müller, C.; Epding, B.; Kowalsky, W.; Kronik, L.; Snaith, H. J.; Pucci, A.; Lovrinčić, R. Optical Phonons in Methylammonium Lead Halide Perovskites and Implications for Charge Transport. *Mater. Horiz.* **2016**, *3*, 613.

(24) Saran, R.; Heuer-Jungemann, A.; Kanaras, A. G.; Curry, R. J. Giant Bandgap Renormalization and Exciton-Phonon Scattering in Perovskite Nanocrystals. *Adv. Opt. Mater.* **2017**, *5*, 1700231.

(25) Frost, J. M.; Whalley, L. D.; Walsh, A. Slow Cooling of Hot Polarons in Halide Perovskite Solar Cells. *ACS Energy Lett.* **2017**, *2*, 2647−2652.

(26) McClure, E. T.; Ball, M. R.; Windl, W.; Woodward, P. M. $Cs_2AgBiX6$ (X = Br, Cl): New Visible Light Absorbing, Lead-Free

DOI: 10.1021/acsnano.8b02936
ACS Nano 2018, 12, 8081−8090

Halide Perovskite Semiconductors. *Chem. Mater.* **2016**, *28*, 1348−1354.
(27) Filip, M. R.; Hillman, S.; Haghighirad, A. A.; Snaith, H. J.; Giustino, F. Band Gaps of the Lead-Free Halide Double Perovskites $Cs_2BiAgCl_6$ and $Cs_2BiAgBr_6$ from Theory and Experiment. *J. Phys. Chem. Lett.* **2016**, *7*, 2579−2585.
(28) Ke, X.; Yan, J.; Zhang, A.; Zhang, B.; Chen, Y. Optical Band Gap Transition from Direct to Indirect Induced by Organic Content of $CH_3NH_3PbI_3$ Perovskite Films. *Appl. Phys. Lett.* **2015**, *107*, 091904.
(29) Yang, J.; Zhang, P.; Wei, S.-H. Band Structure Engineering of $Cs_2AgBiBr_6$ Perovskite through Order-Disordered Transition: A First-Principle Study. *J. Phys. Chem. Lett.* **2018**, *9*, 31−35.
(30) Filip, M. R.; Liu, X.; Miglio, A.; Hautier, G.; Giustino, F. Phase Diagrams and Stability of Lead-Free Halide Double Perovskites $Cs_2BB'X6$, B = Sb, Bi, B′ = Cu, Ag, Au and X = Cl, Br, I. *J. Phys. Chem. C* **2018**, *122*, 158−170.
(31) Perdew, J. P.; Ruzsinszky, A.; Csonka, G. I.; Vydrov, O. A.; Scuseria, G. E.; Constantin, L. A.; Zhou, X.; Burke, K. Restoring the Density-Gradient Expansion for Exchange in Solids and Surfaces. *Phys. Rev. Lett.* **2008**, *100*, 136406.
(32) Smit, W. M.; Dirksen, G. J.; Stufkens, D. J. Infrared and Raman Spectra of the Elpasolites $Cs_2NaSbCl_6$ and $Cs_2NaBiCl_6$: Evidence for a Pseudo Jahn-Teller Distorted Ground State. *J. Phys. Chem. Solids* **1990**, *51*, 189−196.
(33) Krylov, A. S.; Vtyurin, A. N.; Bulou, A.; Voronov, V. N. Raman Spectra and Phase Transitions in the Rb_2KScF_6 Elpasolite. *Ferroelectrics* **2003**, *284*, 47−64.
(34) Papatheodorou, G. N. Raman Spectroscopic Studies of Yttrium (III) Chloride-Alkali Metal Chloride Melts and of Cs_2NaYCl_6 and YCl_3 Solid Compounds. *J. Chem. Phys.* **1977**, *66*, 2893−2900.
(35) Valakh, M. Y.; Lisitsa, M. P.; Peresh, E. Y.; Trylis, O. V.; Yaremko, A. M. The Raman Spectra of the Family Crystals $Cs_3Bi_2Br_9$, $Rb_3Bi_2Br_9$ and $Rb_3Sb_2Br_9$. *J. Mol. Struct.* **1997**, *436*−*437*, 309−313.
(36) de Jong, M.; Seijo, L.; Meijerink, A.; Rabouw, F. T. Resolving the Ambiguity in the Relation Between Stokes Shift and Huang-Rhys Parameter. *Phys. Chem. Chem. Phys.* **2015**, *17*, 16959−16969.
(37) Artús, L.; Cuscó, R.; Martín, J. M.; González-Díaz, G. Up to Fifth-Order Raman Scattering of InP Under Nonresonant Conditions. *Phys. Rev. B: Condens. Matter Mater. Phys.* **1994**, *50*, 11552−11555.
(38) Zhang, Q.; Zhang, J.; Utama, M. I.; Peng, B.; De La Mata, M.; Arbiol, J.; Xiong, Q. Exciton-Phonon Coupling in Individual ZnTe Nanorods Studied by Resonant Raman Spectroscopy. *Phys. Rev. B: Condens. Matter Mater. Phys.* **2012**, *85*, 085418.
(39) Zeyher, R. Theory of Multiphonon Raman Spectra Above the Energy Gap in Semiconductors. *Solid State Commun.* **1975**, *16*, 49−52.
(40) Rudin, S.; Reinecke, T. L. Temperature-Dependent Exciton Linewidths in Semiconductor Quantum Wells. *Phys. Rev. B: Condens. Matter Mater. Phys.* **1990**, *41*, 3017−3027.
(41) Fang, H.-h.; Wang, F.; Adjokatse, S.; Zhao, N.; Even, J.; Loi, M. A. Photoexcitation Dynamics in Solution-Processed Formamidinium Lead Iodide Perovskite Thin Films for Solar Cell Applications. *Light: Sci. Appl.* **2016**, *5*, e16056.
(42) Yu, P. D. P. Y.; Dr, P.; Cardona, D. h. c. M. *Fundamentals of Semiconductors*; Springer: Berlin, Germany, 2010; pp 107−158.
(43) Frost, J. M. Calculating Polaron Mobility in Halide Perovskites. *Phys. Rev. B: Condens. Matter Mater. Phys.* **2017**, *96*, 195202.
(44) Zhao, X. G.; Yang, J. H.; Fu, Y.; Yang, D.; Xu, Q.; Yu, L.; Wei, S. H.; Zhang, L. Design of Lead-Free Inorganic Halide Perovskites for Solar Cells *via* Cation-Transmutation. *J. Am. Chem. Soc.* **2017**, *139*, 2630−2638.
(45) Biaggio, I. Mobility of an Electron in a Multimode Polar Lattice. *Phys. Rev. B: Condens. Matter Mater. Phys.* **1999**, *60*, 299−307.
(46) Zhu, H.; Miyata, K.; Fu, Y.; Wang, J.; Joshi, P. P.; Niesner, D.; Williams, K. W.; Jin, S.; Zhu, X. Y. Screening in Crystalline Liquids Protects Energetic Carriers in Hybrid Perovskites. *Science* **2016**, *353*, 1409−1413.
(47) Yang, B.; Chen, J.; Yang, S.; Hong, F.; Sun, L.; Han, P.; Pullerits, T.; Deng, W.; Han, K. Lead-Free Silver-Bismuth Halide Double Perovskite Nanocrystals. *Angew. Chem., Int. Ed.* **2018**, *57*, 5359−5363.
(48) Neukirch, A. J.; Nie, W.; Blancon, J. C.; Appavoo, K.; Tsai, H.; Sfeir, M. Y.; Katan, C.; Pedesseau, L.; Even, J.; Crochet, J. J.; Gupta, G.; Mohite, A. D.; Tretiak, S. Polaron Stabilization by Cooperative Lattice Distortion and Cation Rotations in Hybrid Perovskite Materials. *Nano Lett.* **2016**, *16*, 3809−3816.
(49) Santomauro, F. G.; Grilj, J.; Mewes, L.; Nedelcu, G.; Yakunin, S.; Rossi, T.; Capano, G.; Al Haddad, A.; Budarz, J.; Kinschel, D.; Ferreira, D. S.; Rossi, G.; Tovar, M. G.; Grolimund, D.; Samson, V.; Nachtegaal, M.; Smolentsev, G.; Kovalenko, M. V.; Chergui, M. Localized Holes and Delocalized Electrons in Photoexcited Inorganic Perovskites: Watching Each Atomic Actor by Picosecond X-ray Absorption Spectroscopy. *Struct. Dyn.* **2017**, *4*, 044002.
(50) Ning, W.; Wang, F.; Wu, B.; Lu, J.; Yan, Z.; Liu, X.; Tao, Y.; Liu, J.-M.; Huang, W.; Fahlman, M.; Hultman, L.; Sum, T. C.; Gao, F. Long Electron-Hole Diffusion Length in High-Quality Lead-Free Double Perovskite Films. *Adv. Mater.* **2018**, *30*, 1706246.
(51) Pantaler, M.; Cho, K. T.; Queloz, V. I. E.; Benito, I. G.; Fettkenhauer, C.; Anusca, I.; Nazeeruddin, M. K.; Lupascu, D. C.; Grancini, G. Hysteresis-Free Lead-Free Double-Perovskite Solar Cells by Interface Engineering. *ACS Energy Lett.* **2018**, *3*, 1781−1786.
(52) Guzelturk, B.; Belisle, R. A.; Smith, M. D.; Bruening, K.; Prasanna, R.; Yuan, Y.; Gopalan, V.; Tassone, C. J.; Karunadasa, H. I.; McGehee, M. D.; Lindenberg, A. M. Terahertz Emission from Hybrid Perovskites Driven by Ultrafast Charge Separation and Strong Electron-Phonon Coupling. *Adv. Mater.* **2018**, *30*, 1704737.
(53) Eßer, F.; Drachenko, O.; Patanè, A.; Ozerov, M.; Winnerl, S.; Schneider, H.; Helm, M. Direct Determination of the Electron Effective Mass of GaAsN by Terahertz Cyclotron Resonance Spectroscopy. *Appl. Phys. Lett.* **2015**, *107*, 062103.
(54) Kresse, G.; Furthmüller, J. Efficient Iterative Schemes for *ab initio* Total-Energy Calculations using a Plane-Wave Basis Set. *Phys. Rev. B: Condens. Matter Mater. Phys.* **1996**, *54*, 11169−11186.
(55) Kresse, G.; Furthmüller, J. Efficiency of *ab-initio* Total Energy Calculations for Metals and Semiconductors using a Plane-Wave basis Set. *Comput. Mater. Sci.* **1996**, *6*, 15−50.
(56) Togo, A.; Tanaka, I. First Principles Phonon Calculations in Materials Science. *Scr. Mater.* **2015**, *108*, 1−5.

DOI: 10.1021/acsnano.8b02936
ACS Nano 2018, 12, 8081−8090